Coercivity limits in nanoscale ferromagnets

Jeotikanta Mohapatra,[1,*] J. Fischbacher,[2,3,*] M. Gusenbauer,[2,3] M. Y. Xing,[1] J. Elkins,[1] T. Schrefl,[2,3,†] and J. Ping Liu[1,‡]

[1]*Department of Physics, University of Texas at Arlington, Arlington, Texas 76019, USA*

[2]*Christian Doppler Laboratory for Magnet Design Through Physics Informed Machine Learning, Viktor Kaplan-Straße 2E, 2700 Wiener Neustadt, Austria*

[3]*Department for Integrated Sensor Systems, Danube University Krems, Viktor Kaplan-Straße 2E, 2700 Wiener Neustadt, Austria*

(Received 2 January 2022; revised 10 March 2022; accepted 6 June 2022; published 24 June 2022)

It has been a puzzle for a century about how "hard" (coercive) a ferromagnet can be. Seven decades ago, W. Brown gave his famous theorem to correlate coercivity of a ferromagnet to its magnetocrystalline anisotropy field. However, the experimental coercivity values are far below the calculated level given by the theorem, which is called Brown's Coercivity Paradox. The paradox has been considered to be related to the complex microstructures of the magnets in experiments because coercivity is an extrinsic property that is sensitive to any imperfections in the specimens. To date, coercivity cannot be predicted and calculated by quantitative modeling. In this investigation, we carried out a case study on the high magnetic coercivity of Co nanowires exceeding the magnetocrystalline anisotropy field as predicted by Brown's theorem. It is found that the aspect ratio and diameter of the nanocrystals have a strong effect on the coercivity. When the nanocrystals have an increased aspect ratio, the coercivity is significantly higher than the magnetocrystalline anisotropy field of a hcp Co crystal. Micromagnetic simulations give a coercivity aspect-ratio dependence that is well consistent with the experimental results. It is also revealed that a coercivity limit exists based on the geometrical structures of the nanocrystals that govern the demagnetizing process. The quantitative correlation obtained between the structure and coercivity enables material design of advanced permanent magnets in the future.

DOI: 10.1103/PhysRevB.105.214431

I. INTRODUCTION

Ferromagnetic materials possessing a permanent magnetization in the absence of an external magnetic field are fundamentally important for many advanced technologies and devices [1–4]. Their most important characteristic is the magnetic hysteresis in response to an external field, which is usually described by the saturation magnetization (M_S) and the coercivity (H_{ci}) as the major parameters. The M_S for a given material is an *intrinsic* property. The H_{ci} is an *extrinsic* property, and its value strongly relates not only to the crystalline and electronic structures but also to the microstructural and proximity parameters [5,6]. Therefore, coercivity and its mechanisms in permanent magnets have always been an intensive research topic.

Significant efforts have been made over the last century to understand coercivity mechanisms in order to develop high coercivity for practical applications. However, the experimental coercivity values are found to be much lower than the theoretical level set by W. Brown's theorem proposed in the 1940s [7]. According to Brown, the coercive field in a perfectly homogenous continuum magnet of ellipsoid shape is given by [7,8]

$$\mu_0 H_{ci} \geqslant \frac{2K_1}{M_S} - N_d M_S, \tag{1}$$

where μ_0, K_1, and N_d are the permeability of vacuum, the magnetocrystalline anisotropy constant, and the demagnetizing factor, respectively. Equation (1) is referred as Brown's theorem, applicable when K_1 is positive and significant to warrant a positive $\mu_0 H_{ci}$ [9,10]. The first term on the right side of the equation corresponds to the magnetocrystalline anisotropy field (H_a), while the second term represents the demagnetizing field.

However, experimental results in the past century are far below the level predicted by this formula (only 20%–40% of the corresponding anisotropy field values, no matter what the specimen shape was used), which is known as the Brown's paradox [11–13]. Recently, a significant enhancement in the coercivity value in nanoscale hard magnetic materials has been achieved [14,15] including a notable example of $L1_0$-FePt nanocrystals with a room-temperature coercivity of 70 kOe [16], which is about 60% of the corresponding H_a.

The paradox has been considered to be related to the complex microstructures of the magnets in experiments because coercivity as an extrinsic property is sensitive to any imperfections in the specimens. To account for the extrinsic parameter effects on the coercivity, Kronmüller added a fractional coefficient to Brown's formula, leading to a phenomenological model that fits the experimental data quite well. However, the model does not provide quantitative information about the microstructural effects and remains an empirical treatment [8,9].

In our recent experimental work, we have obtained magnetic coercivity in hcp-structured cobalt nanowires

*These authors contributed equally to this work.
†Corresponding author: thomas.schrefl@donau-uni.ac.at
‡Corresponding author: pliu@uta.edu

higher than the magnetocrystalline anisotropy field, verifying Brown's theorem [17–20]. Nevertheless, it is yet unknown how the magnetocrystalline anisotropy and the shape anisotropy contributed to the high coercivity. To gain further understanding of the coercivity mechanisms, we carry out a comprehensive investigation of the coercivity mechanisms by combining experimental and theoretical studies to obtain quantitative correlations between the geometrical parameters (aspect ratio and diameter) and the coercive force, particularly to quantify the demagnetizing field effect at the nanoscale.

II. EXPERIMENTAL AND COMPUTATIONAL DETAILS

A. Sample preparation

For the preparation of high-aspect-ratio Co nanocrystals, 1 g of Co(II) laurate, 6 mg of $RuCl_3$, and 0.2–1.0 g of hexadecylamine (HDA) were added to 15 ml of 1,2 butanediol in a glass reactor. The glass reactor was purged with forming gas (Ar93% + $H_2$7%) for 5 min and then sealed with a rubber stopper. A rubber balloon sealed with a syringe was inserted into the stopper to maintain a small positive pressure with forming gas in the glass reactor. Afterwards, the enclosure was placed in an ultrasonic water bath adjusted to 65 °C. The contents within the enclosure were then mixed for 60 min using ultrasonication. Then the reaction mixture was heated for 15 min at 240 °C. After the reaction, the solution was cooled to room temperature and the obtained, black-colored precipitates were washed and centrifuged several times with chloroform. The HDA to $RuCl_3$ ratio was controlled by adjusting the amount of HDA added while keeping the $RuCl_3$ content constant. This synthesis procedure can be scaled up to the multigram level without sacrificing uniformity. To synthesize 5 g of Co nanowires, 40 g of Co(II) laurate, 0.12 g of $RuCl_3$, and 10 g of HDA were added to 300 ml of 1,2 butanediol in a 2 liter glass reactor.

Synthesizing hcp-structured Co nanocrystals with uniaxial magnetocrystalline anisotropy is difficult because the fcc phase of cobalt is more stable than the hcp phase when the average particle size is smaller than 20 nm [21]. In this study we modified the previously described synthesis process to prepare monodispersed, hcp-structured Co nanoparticles [17]. In a typical synthesis of 10 nm Co nanocrystals, 1 g (2 mmol) of cobalt (II) laurate, 2 g (8 mmol) of HDA, and (60 mg) $RuCl_3$ were dissolved in 30 ml of 1, 2 butanediol in a Teflon-lined stainless-steel hydrothermal reactor. The Teflon bottle was purged with forming gas for 5 min and then placed in an ultrasonic water bath adjusted to 65 °C for 60 min. Then the Teflon bottle was transferred to an autoclave reactor and heated at 250 °C for 75 min. The increase in the Ru content leads to the formation of dodecahedral nanoparticles with the smallest distribution of nanoparticles in size.

B. Characterization techniques

To study the morphology and crystal structure of Co nanocrystals, transmission electron microscope (TEM) micrographs were taken with a Hitachi H-9500 TEM operating at 300 kV. The morphology of the aligned Co nanocrystals was recorded using Hitachi S-4800 II Field Emission Scanning Electron Microscopy (FE-SEM). The phase of the synthesized nanocrystals was investigated using x-ray powder diffraction from a Rigaku Ultima IV with a CuK_α source. The aligned Co nanocrystal assemblies were produced in epoxy resin to measure the magnetic properties. The Co nanocrystals were first dispersed in chloroform, and then a certain amount of epoxy resin was injected into the Co nanocrystal dispersion. The nanocrystals were uniformly dispersed in epoxy at a concentration of 5–10 wt% to eliminate magnetic interactions between neighboring nanocrystals. After that, the composite was put into a mold and allowed to cure in a 2.0 T external magnetic field. The magnetic properties of the samples were studied using a physical property measurement system (Quantum Design DynaCool-PPMS).

C. Micromagnetic calculation

We applied a modified Sharrock's equation [22,23] for the coercive field as outlined by Forster and co-workers [24] to calculate the coercivities of elongated Co particles. We approximated the coercive field by

$$H_c = H_{sw,0}\left(1 - \sqrt{\frac{k_B T}{(K_1 + K_d)V_{eff}}\ln\frac{f_0 t}{\ln 2}}\right). \tag{2}$$

Here V_{eff} denotes the effective volume of the reversed nucleus. K_1 is the magneto-crystalline anisotropy constant, whereby we assume that the magneto-crystalline anisotropy axis is parallel to the long axis of the particle. $K_d = \frac{1}{2}\mu_0 M_s^2(N_\perp - N_\parallel)$ accounts for the particle shape; $N_\parallel$ and $N_\perp$ are the demagnetizing factors for the magnetization parallel and perpendicular to the long axis. $H_{sw,0} = \frac{1}{(\sin^{2/3}\theta+\cos^{2/3}\theta)^{3/2}}\frac{2(K_1+K_d)}{\mu_0 M_s}$ is the switching field without thermal activation. θ is the angle of the field with respect to the long axis of the particle. Based on micromagnetic simulations of the minimum energy path for magnetization reversal, the effective volume of the reversed nucleus was estimated as

$$V_{eff} = \frac{1}{L}\left(D + \sqrt{\frac{A}{K_1 + \mu_0 M_s^2/2}}\right)V. \tag{3}$$

V, L, and D are particle volume, the particle length, and the particle diameter, respectively; A is the exchange constant. In Eq. (2) we used $f_0 = 7.2 \times 10^{10}$ Hz and a measuring time $t = 1$ s. Please note that Eq. (2) does not follow from a rigorous derivation. Rather than that, we modified Sharrock's equation guided by observations of micromagnetic results for thermally activated switching. For computing the coercive fields, we sampled the particle diameter and the particle length from a Gaussian distribution according to the experimental mean and standard deviations. The intrinsic properties used for the simulations were $K_1 = 0.45\,\mathrm{MJ/m^3}$, $A = 13\,\mathrm{pJ/m}$, and $\mu_0 M_s = 1.76\,\mathrm{T}$.

To compute the magnetization reversal path, we used the string method within the framework of a finite element micromagnetic solver [25]. The magnetic states were computed for Co cylinders of three different aspect ratios using an external field that gives an energy barrier of $25\,k_B T$. The external field is applied at an angle of 17.6° with respect to the long axis of the cylinder. Here k_B is the Boltzmann constant, and the temperature T was 300 K.

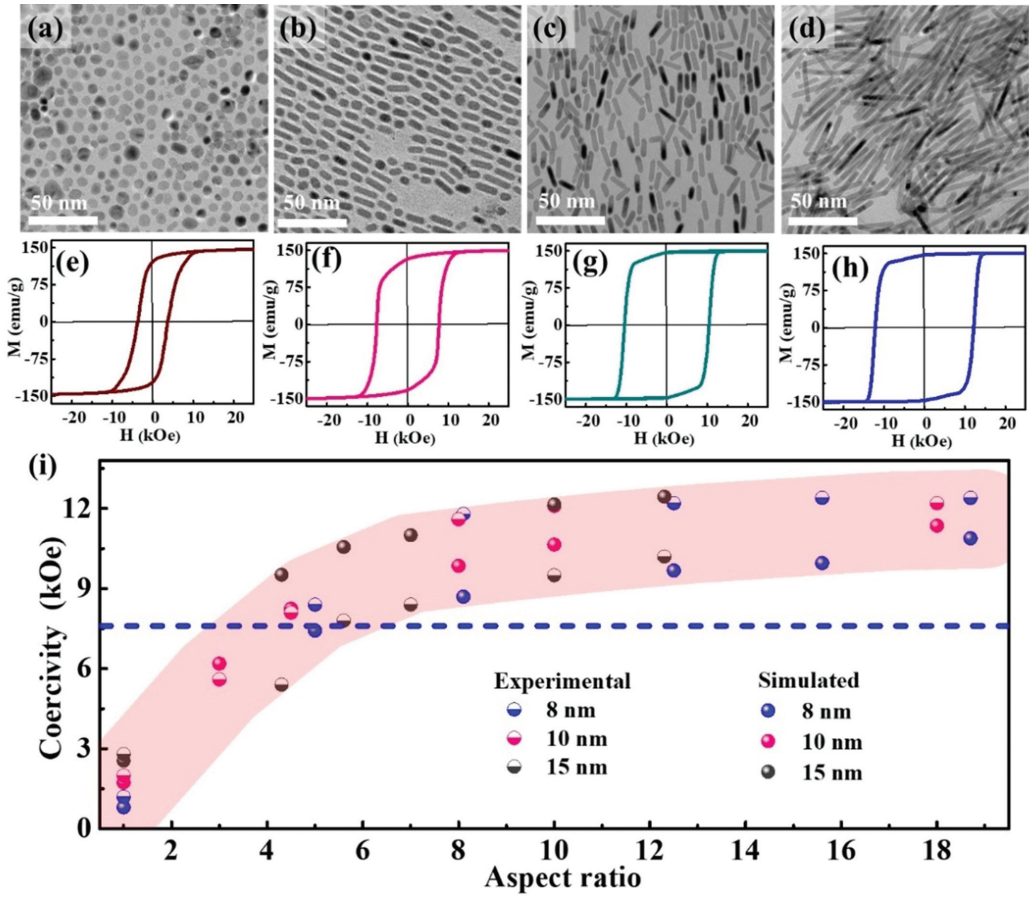

FIG. 1. Aspect ratio dependence coercivity value in Co nanocrystals. (a)–(d) TEM images and (e)–(h) the corresponding hysteresis loops at room temperature of Co nanocrystals with aspect ratios of ∼1, ∼3, ∼5, and ∼10, respectively, where the average diameter of the nanocrystals is about 10 nm. (i) Aspect ratio dependence of coercivity. The full symbols in (i) are the results of a coercivity model, which is based on the micromagnetic simulation of switching over a nonzero energy barrier. The blue dashed line represents the magnetocrystalline anisotropy field of hcp Co.

III. RESULTS AND DISCUSSION

A. The aspect-ratio effect

We developed a well-controllable and scalable thermal decomposition process to synthesize hcp Co nanocrystals with precise control of the diameter and aspect ratio. Figure 1 shows the representative TEM images and the corresponding room-temperature hysteresis loops as well as coercivity values of different aspect-ratio hcp Co nanocrystals. The coercivity value for their aligned assemblies increases from 2 to 12.1 kOe as the aspect ratio increases from 1 to 10 while maintaining the diameter of approximately 10 nm [see Figs. 1(a)–1(h)]. The record high coercivity in the high-aspect-ratio Co nanowires is ascribed to perfect single-crystalline structures and magnetization easy axis orientation along the long axis of nanowires, as revealed in our earlier work [17–20]. X-ray diffraction and high-resolution TEM results also confirm that the wires have an hcp crystal structure, and each wire is a single crystal with the c axis (002), or the easy magnetization direction is along the wire's long axis. See Fig. S1 in the Supplemental Material [26] for high-resolution TEM analysis.

Although a high coercivity is achieved in the high-aspect-ratio Co NWs, the coercivity is still only about 73% of the theoretical effective magnetic anisotropy field (16.5 kOe, the sum of magnetocrystalline and shape anisotropy field of cobalt) [27]. To determine the practical coercivity limit as well as quantify how the coercivity is related to the aspect ratio, we carried out a systematic simulation based on the minimum energy path method of micromagnetics [24] for the finite geometry nanocrystal. A detailed illustration of the simulation method can be found in the experimental and computational details. As seen in Fig. 1(i), the simulated coercivity values are in good agreement with the experimental coercivity data, showing a direct correlation to the aspect ratio (p; average length to diameter ratio). Both results are higher than the magnetocrystalline anisotropy field (∼7.6 kOe [28]) of Co material when p is larger than 4 [29,30], in agreement with Brown's theorem. When p is less than 4, a rapid decrease in coercivity takes place with decreasing aspect ratio, which accords with the hypothesis of a larger demagnetizing field along the magnetization easy axis, especially for equiaxed nanocrystals (where $p = 1$, $N_d = 1/3$). Furthermore, the red belt in Fig. 1(i) can be regarded as a coercivity ceiling (by taking account of errors in coercivity data obtained from experiments and simulations).

Figure 1(i) shows that the coercivity model qualitatively explains the dependence of coercivity on aspect ratio. To

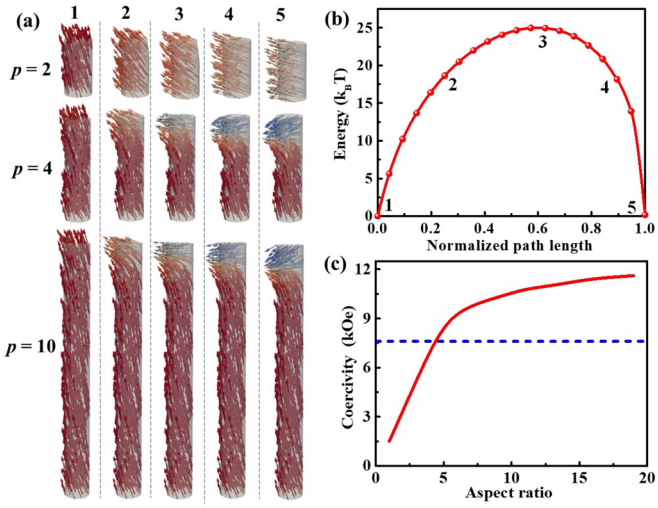

FIG. 2. Magnetization reversal and coercivity of high-aspect-ratio Co nanocrystals with diameter of 10 nm. (a) The magnetic states along the minimum energy path for Co nanocrystals with $p = 2$, 4, and 10. (b) Energy along the minimum energy path for Co nanocrystals with aspect ratio $p = 2$. The external field is applied at 17.6° with respect to the long axis. The field strength is such that the energy barrier is $25\,k_B$T. (c) The aspect ratio dependence of the simulated coercivity of Co nanowires with diameter of 10 nm.

understand how the magnetization reversal occurs, we carried out detailed micromagnetic simulations of the minimum energy path and angular dependence of experimental coercive and switching fields. First, we computed how the system passes over the lowest saddle point and recorded the associated magnetic states (see the experimental and computational section for a detailed illustration of the simulation). Figure 2(a) shows how the nanocrystals with different aspect ratios reverse under the action of an applied field and thermal fluctuations. The magnetization starts at a local minimum (state 1) [see Fig. 2(b) and Fig. S2 in the Supplemental Material [26]], proceeds through the saddle point configuration (state 3), and then continues through states 4 and 5 after crossing the saddle point. The reversal of nanocrystals with $p = 2$ occurs through uniform rotation, as can be seen from the magnetization distribution at the saddle point, whereas the magnetization distribution of nanocrystals with $p = 4$ and $p = 10$ differs considerably from that of nanocrystals with $p = 2$. Unlike magnetization rotation that is usually expected in single-domain and single-crystalline ultrathin nanorods and nanowires, our simulation reveals that localized nucleation and subsequent domain expansion cause the magnetization reversal, especially when the $p \geqslant 4$. The images shown in Fig. 2(a) are the magnetization configurations along the minimum energy path. The minimum energy path connects two stable states, here the magnetic state before and after magnetization reversal, in such a way that if, for any point along the path, the gradient of the energy is parallel to the path [31]. The sequence of magnetic states along the minimum path shows the most likely magnetization reversal process under the influence of thermal activations. The arrows in the images represent the magnetization vectors, and the color refers to projection of the magnetization along the long axis of the particle. It can be seen that for $p \geqslant 4$ the magnetization reversal is nonuniform. A reversed nucleus forms locally near one end of the particle. The images of the magnetization patterns are labeled with numbers that denote the position of the state along the minimum energy path given by Fig. 2(b).

Furthermore, the simulation of the minimum energy path over the saddle point [see Fig. 2(a)] shows that the magnetization reversal involves a finite volume where the magnetization starts to deviate from the easy axis. This volume in which magnetization reversal is initiated is much smaller than the particle volume and is referred to as the effective volume [32]. In nonellipsoidal particles, localized reversal is caused by nonuniform demagnetizing fields near the ends [33,34]. The saddle point configurations are labeled with number 3. To estimate the volume associated with the magnetization in the nucleus, we look at where the magnetization component parallel to the long axis of the wire, m_z, becomes negative. The volume for which $m_z < 0$ at the saddle point is 104 nm³ for $p = 4$ and 116 nm³ for $p = 10$. For a fixed diameter, the effective volume associated with the reversed nucleus increases with nanocrystal length [24,35], resulting in an increase in effective magnetic anisotropy, and, as a result, coercivity value increases with aspect ratio up to $p = 10$ [see Fig. 2(c)]. For a larger aspect ratio ($p > 10$), however, the effective volume of the nucleus is not sensitive to p, because once a certain aspect ratio is reached, a further increase of the particle length does not change the dependence of the energy barrier with the applied field. Therefore, the effective volume of the nucleus remains constant with increasing p [24], and coercivity, H_c, saturates with increasing p. The simulated coercivity data shown in Fig. 2(c) show that the slope of $H_c(p)$ flattens out after reaching an aspect ratio of $p = 10$.

The simulations, which were performed for a single nanocrystal without taking into account distributions, reveal that in small aspect ratio nanocrystals, magnetization reversal occurs through rotation, while in high-aspect-ratio nanocrystals, it occurs through localized nucleation and subsequent domain expansion. The effective volume associated with magnetization reversal increases significantly with increasing aspect ratio up to $p = 10$, resulting in an increase in effective magnetic anisotropy, which explains why, as shown in Fig. 2(c), the coercivity value increased with increasing aspect ratio. We found a good consistency between the experimental and theoretical coercivity data; we almost reached the coercivity limit determined by the micromagnetic modeling. One can conclude that the Brown theorem is proved hereafter, and the experimental coercivity matches the micromagnetic modeling that can be considered as the coercivity limit.

To compare the theoretical results on the reversal process with the experiment, we have measured the angular dependence of coercivity and switching fields for Co nanowires of diameter 10 nm and aspect ratio 10 and compared them with the analytical curves computed based on the Stoner-Wohlfarth (S-W) model [36,37], which predicts the angular dependence of magnetic hysteresis in single-domain particles with uniaxial anisotropy, as shown in Fig. 3. The experimental coercivity is found to be in good consistency with the S-W rotation mode [see Fig. 3(a)], which shows a dramatic drop in coercivity near 90° (hard axis, i.e., normal to the NWs). The polar plot of the switching field also follows the S-W

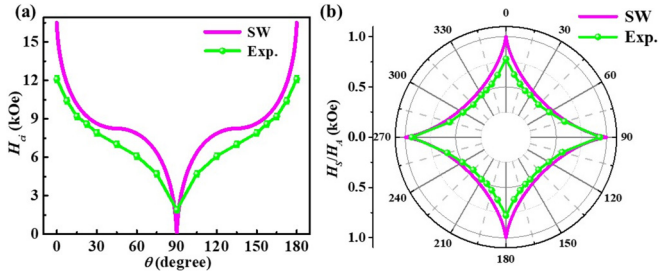

FIG. 3. Comparison between the experimental and analytical angular dependence of (a) coercivity and (b) switching field for nanowires with diameter 10 nm and aspect ratio 11. The pink line in (a) and (b) corresponds to the analytical plots calculated using the S-W model, and green lines represent the experimental data obtained from angular-dependent magnetization curves.

asteroid [see Fig. 3b)]. The angular dependence of coercivity and switching fields indicates that the magnetization reversal in nanowires follows the S-W rotation model even with nonuniform magnetization distribution. Similar behavior has been observed before in recording media [38] and single-domain nanocrystals [19], where nonuniform switching is observed but the coercivity and switching field follow the S-W rotation mode. As a result of combined effects of magnetocrystalline anisotropy and shape anisotropy, as well as S-W rotation-like magnetization reversal, a pronounced coercivity of 12.1 kOe is achieved in the Co NWs. A Stoner-Wohlfarth-like behavior of the angular dependence of the switching field is a clear indication that a high coercive field has been achieved [39] and that the size of local defects in the magnetocrystalline anisotropy is diminished [40].

B. The diameter effect

The next question is how high the coercivity can be if we have equiaxed nanocrystals, where the demagnetizing field is same along all the directions. At the same time to establish a correlation between coercivity and diameter, we have synthesized dodecahedral-shaped Co nanocrystals (see SEM micrograph in Fig. S3 in Supplemental Material [26]) with an average diameter of 8 to 22 nm. Figure 4 shows the representative TEM micrographs and the corresponding room-temperature hysteresis loops of the Co nanocrystals with diameters of 8, 12, and 18 nm. It is seen that the coercivity value for the nanocrystals is strongly dependent on the diameter, and an optimum value of coercivity is obtained for 12 nm Co nanocrystals. Unlike the high aspect-ratio nanocrystals, the coercivity values of all the dodecahedral-shaped nanocrystals are lower than the magnetocrystalline anisotropy field of hcp Co materials (7.6 kOe [28]). When we compared our experimental coercivity to the previously published results [41–46], we found that the coercivity obtained in this study is nearly 4–5 times higher. In the following, we will show what causes the high coercivity in the synthesized Co nanoparticles based on structural analysis and detailed micromagnetic simulations.

As stated earlier, the fcc of phase cobalt is more stable than the hcp phase of cobalt, particularly when the average particle size is less than 20 nm [21]. Because the former has a lower magnetocrystalline anisotropy, the formation of the

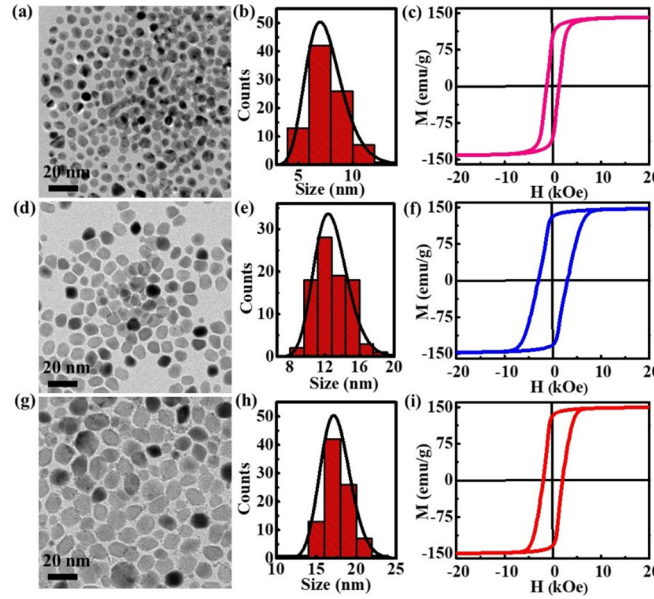

FIG. 4. Diameter dependence of magnetic properties in dodecahedral-shaped Co nanocrystals. TEM images, the corresponding histograms of diameter, and the respective room temperature hysteresis loops of Co nanocrystals with average diameter of (a)–(c) 8 nm, (d)–(f) 12 nm, and (g)–(i) 18 nm, respectively.

fcc phase always leads to reduced coercivity. In this study, to prevent the formation of the fcc phase, a Ru promoter, which is known for passivating the surface energy of exposed facets in hcp-structured Co nanocrystals [47], has been used. The x-ray diffraction pattern of the nanocrystal assemblies and high-resolution TEM micrograph are shown in Fig. 5. Both the analyses confirm the formation of pure hcp-structured Co nanocrystals. Particularly, the high-resolution TEM micrograph reveals prominent lattice fringes that match (002) orientation of hcp Co, which excludes the presence of any impurity phase such as CoO. The intact crystallinity as evidenced by high-resolution TEM and XRD studies appears to be the cause of the high coercivity of 3.1 kOe in the synthesized Co nanoparticles.

To understand the relationship between coercivity and nanocrystals diameter in detail, we have carried out a

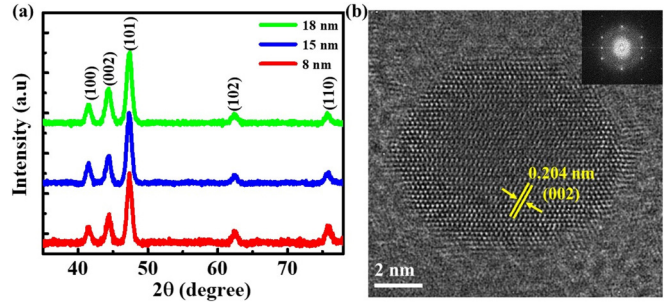

FIG. 5. Structural characterization of dodecahedral-shaped Co nanocrystals. (a) XRD pattern of the Co nanocrystals with different sizes. (b) High-resolution TEM micrograph of a single Co nanocrystal, and inset the corresponding numerical fast Fourier transform (FFT) pattern.

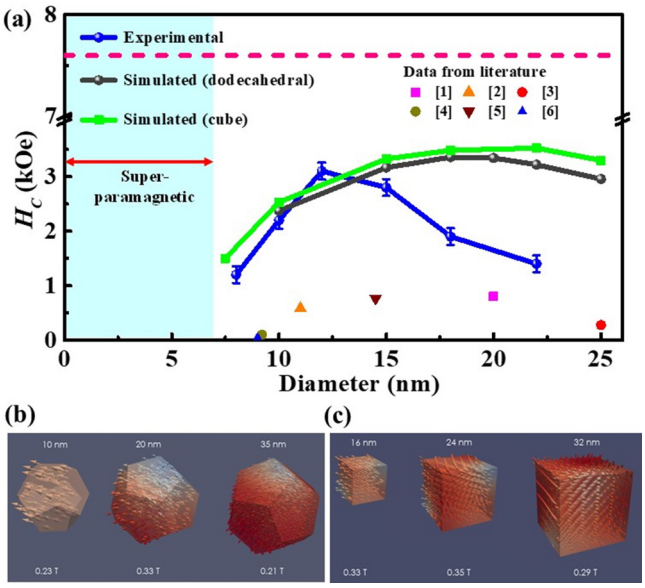

FIG. 6. Diameter dependence of coercivity in dodecahedral-shaped Co nanocrystals. (a) Comparison of experimental coercivity data obtained from this study and the literature [41–46] with the simulated coercivity values. The upper dashed red line represents the magnetocrystalline anisotropy field of cobalt materials. (b), (c) The magnetic states show the computed configuration of the magnetization for the saddle point, at which the energy barrier reaches $25\,k_BT$.

systematical simulation based on the experimental results, as shown in Fig. 6. The experimental coercivity values are found to be very consistent with the simulation findings. The simulated coercivity values can be considered the upper limit of the coercive force [22] since the simulations are based on the assumption that the nanoparticles have perfect crystallinity. When we compared experimental coercivity data from the literature [41–46] and the values obtained in this work with the simulated coercivity (black line and green line), we found that only the experimental coercivity values from this study coincide with the simulated coercivity line. However, both the experimental and simulated coercivity values are lower than the magnetocrystalline anisotropy field. This reduction of coercivity has to be attributed to thermal fluctuations and local demagnetizing fields. With decreasing particle size, the coercivity decreases according to Eq. (2). With increasing particle size, inhomogeneous reversal will occur, which lowers the coercive field. The nanoparticle edges cause a nonuniform demagnetizing field unless the particle is a perfect sphere or ellipsoid. The nonuniform demagnetizing field causes the total field acting locally to be strongly oblique to the easy axis. According to Stoner-Wohlfarth, this causes a decrease in the switching field [39,40,48]. In regions where the total field H (sum of external field and demagnetizing field) is not parallel to the easy axis, the torque M × H is stronger than in the remainder of the magnet. This causes the magnetization to rotate first near the edges or corners. As a consequence, magnetization reversal is not perfectly uniform, resulting in a lower coercivity than the magnetocrystalline anisotropy field. Meanwhile, our experimental results revealed that the theoretical coercivity value in magnetic systems can be approachable with proper control of phase crystallinity and geometrical structures (including size and shape). In Fig. 6(a) we also noticed that the experimental coercivity value drops rapidly with an increasing diameter above the diameter of 15 nm. Although the exact cause is unknown, we believe it is related to the nanocrystal growth mechanism; possibly the larger diameter nanoparticles comprise multiple crystallites [49] due to increased lauric acid content in the reaction solution.

We have also computed the configuration of the magnetization for the saddle point to understand magnetization reversal in equiaxed nanocrystals. When the diameter of dodecahedral nanoparticles is larger than the coherent limit ($D_{coh} \approx 10$ nm), a nonuniform reversal mode can be expected, as revealed by the micromagnetic simulation [see Fig. 6(b)]. The magnetic state at the saddle point for 20 and 35 nm dodecahedral nanoparticles is nonuniform. In contrast, for nanocrystals with a very small diameter ($D \leqslant D_{coh}$), the saddle point configuration is almost uniform in the whole particle, indicating a high coercivity magnetic configuration. However, because we are approaching the superparamagnetic limit, a decreasing trend in coercivity value can be anticipated, as seen in Fig. 6(a). A similar trend in the coercivity value and magnetization reversal [see Fig. 6(c)] are also noticed in cubic-shaped nanocrystals. It can now be concluded that the diameter of the Co nanocrystals plays a key role in determining the reversal modes, which change from the superparamagnetic to the coherent-like rotation and then to nonuniform reversal as the diameter increases.

IV. CONCLUSIONS

In summary, the experimental and modeling studies on the correlations between the coercivity and the geometric parameters of the Co nanocrystals have proved Brown's theorem on magnetic coercivity. The studies also revealed a coercivity limit which is dependent on the geometrical factors (particularly the aspect ratio and the diameter) that can be experimentally controlled at the nanoscale. These results show that magnetic coercivity can be adjusted by controlling the geometrical parameters. Specifically for the Co nanowires under investigation, the coercivity value exceeds the magnetocrystalline anisotropy field when the aspect ratio is above 4, whereas in smaller aspect-ratio and equiaxed nanocrystals, due to the demagnetizing field along the magnetization easy axis and edges, both experimental and simulated coercivity values are reduced below the magnetocrystalline anisotropy field. These findings of the quantitative structure-property correlations make it possible to calculate, predict, and manipulate the magnetic coercivity of nanoscale magnets, which is a key step in enabling the material design of future high-performance permanent magnets for advanced applications.

The data supporting the results are available in the Supplemental Material [26].

ACKNOWLEDGMENTS

The authors thank the Characterization Center for Materials and Biology, the University of Texas at Arlington, and the Ford URP gift fund for supports. The financial support by the Austrian Federal Ministry for Digital and Economic Affairs,

the National Foundation for Research, Technology and Development and the Christian Doppler Research Association is gratefully acknowledged. The authors declare that they have no competing interests.

[1] O. Gutfleisch, M. A. Willard, E. Brück, C. H. Chen, S. G. Sankar, and J. P. Liu, Adv. Mater. **23**, 821 (2011).
[2] L. H. Lewis and F. Jiménez-Villacorta, Metall. Mater. Trans. A **44**, 2 (2013).
[3] D. J. Sellmyer, M. Zheng, and R. Skomski, J. Phys.: Condens. Matter **13**, R433 (2001).
[4] J. Cui, M. Kramer, L. Zhou, F. Liu, A. Gabay, G. Hadjipanayis, B. Balasubramanian, and D. Sellmyer, Acta Mater. **158**, 118 (2018).
[5] J. Mohapatra and J. P. Liu, *Handbook of Magnetic Materials*, edited by E. Brück (Elsevier, North Holland, 2018), Vol. 27, pp. 1–57.
[6] S. Ener, E. Anagnostopoulou, I. Dirba, L.-M. Lacroix, F. Ott, T. Blon, J.-Y. Piquemal, K. P. Skokov, O. Gutfleisch, and G. Viau, Acta Mater. **145**, 290 (2018).
[7] W. F. Brown, Rev. Mod. Phys. **17**, 15 (1945).
[8] H. Kronmüller and M. Fähnle, *Micromagnetism and the Microstructure of Ferromagnetic Solids* (Cambridge University Press, Cambridge, 2003), pp. 96–102.
[9] J. M. Coey, *Magnetism and Magnetic Materials* (Cambridge University Press, Cambridge, 2010), pp. 244–251.
[10] U. Hartmann, Phys. Rev. B **36**, 2331 (1987).
[11] A. Aharoni, *Introduction to the Theory of Ferromagnetism*, International Series of Monographs on Physics, Vol. 109, 2nd Ed. (Clarendon Press, Oxford, 2000), pp. 113–115.
[12] H. Zijlstra, in *Handbook of Magnetic Materials*, edited by E. P. Wohlfarth (Elsevier, 1986), Vol. 3, pp. 60–63.
[13] B. D. Cullity and C. D. Graham, *Introduction to Magnetic Materials* (John Wiley & Sons, New York, 2011), pp. 369–371.
[14] B. Balasubramanian, P. Mukherjee, R. Skomski, P. Manchanda, B. Das, and D. J. Sellmyer, Sci. Rep. **4**, 6265 (2014).
[15] E. Girt, K. M. Krishnan, G. Thomas, and Z. Altounian, Appl. Phys. Lett. **76**, 1746 (2000).
[16] T. Shima, K. Takanashi, Y. Takahashi, and K. Hono, Appl. Phys. Lett. **85**, 2571 (2004).
[17] K. Gandha, K. Elkins, N. Poudyal, X. Liu, and J. P. Liu, Sci. Rep. **4**, 5345 (2014).
[18] K. Gandha, J. Mohapatra, and J. P. Liu, J. Magn. Magn. Mater. **438**, 41 (2017).
[19] J. Mohapatra, M. Xing, J. Elkins, J. Beatty, and J. P. Liu, Adv. Funct. Mater. **31**, 2010157 (2021).
[20] J. Elkins, J. Mohapatra, M. Xing, J. Beatty, and J. P. Liu, J. Alloys Compd. **864**, 158123 (2021).
[21] O. Kitakami, H. Sato, Y. Shimada, F. Sato, and M. Tanaka, Phys. Rev. B **56**, 13849 (1997).
[22] M. P. Sharrock, J. Appl. Phys. **76**, 6413 (1994).
[23] J.-C. S. Levy, *Magnetic Structures of 2d and 3d Nanoparticles: Properties and Applications* (CRC Press, Boca Raton, FL, 2018), p. 233.
[24] H. Forster, N. Bertram, X. Wang, R. Dittrich, and T. Schrefl, J. Magn. Magn. Mater. **267**, 69 (2003).
[25] J. Fischbacher, A. Kovacs, H. Oezelt, M. Gusenbauer, T. Schrefl, L. Exl, D. Givord, N. M. Dempsey, G. Zimanyi, M. Winklhofer, G. Hrkac, R. Chantrell, N. Sakuma, M. Yano, A. Kato, T. Shoji, and A. Manabe, Appl. Phys. Lett. **111**, 072404 (2017).
[26] See Supplemental Material at http://link.aps.org/supplemental/10.1103/PhysRevB.105.214431 for high-resolution TEM image of Co nanowire, SEM image Co nanoparticles, XRD pattens of Co nanowires, and discussion of magnetization reversal of elongated Co particles for different aspect ratios.
[27] W. F. Brown, Phys. Rev. **105**, 1479 (1957).
[28] R. Skomski and J. M. D. Coey, *Permanent Magnetism* (Taylor & Francis, Philadelphia, 1999), pp. 150–168.
[29] H. Li, Q. Wu, Y. Peng, H. Xu, J. Zhang, and M. Yue, J. Magn. Magn. Mater. **469**, 203 (2019).
[30] H. Li, Q. Wu, M. Yue, Y. Peng, Y. Li, J. Liang, D. Wang, and J. Zhang, J. Magn. Magn. Mater. **481**, 104 (2019).
[31] S. Bance, J. Fischbacher, A. Kovacs, H. Oezelt, F. Reichel, and T. Schrefl, JOM **67**, 1350 (2015).
[32] E. D. Boerner and H. N. Bertram, IEEE Trans. Magn. **33**, 3052 (1997).
[33] A. Holz, Phys. Status Solidi B **25**, 567 (1968).
[34] H. Schmidts, G. Martinek, and H. Kronmüller, J. Magn. Magn. Mater. **104**, 1119 (1992).
[35] S. Bance, J. Fischbacher, T. Schrefl, I. Zins, G. Rieger, and C. Cassignol, J. Magn. Magn. Mater. **363**, 121 (2014).
[36] E. H. Frei, S. Shtrikman, and D. Treves, Phys. Rev. **106**, 446 (1957).
[37] E. C. Stoner and E. Wohlfarth, Philos. Trans. R. Soc. London A **240**, 599 (1948).
[38] R. Dittrich, G. Hu, T. Schrefl, T. Thomson, D. Suess, B. D. Terris, and J. Fidler, J. Appl. Phys. **97**, 10J705 (2005).
[39] S. Bance, B. Seebacher, T. Schrefl, L. Exl, M. Winklhofer, G. Hrkac, G. Zimanyi, T. Shoji, M. Yano, N. Sakuma, M. Ito, A. Kato, and A. Manabe, J. Appl. Phys. **116**, 233903 (2014).
[40] J. Fischbacher, A. Kovacs, L. Exl, J. Kühnel, E. Mehofer, H. Sepehri-Amin, T. Ohkubo, K. Hono, and T. Schrefl, Scr. Mater. **154**, 253 (2018).
[41] O. Margeat, C. Amiens, B. Chaudret, P. Lecante, and R. E. Benfield, Chem. Mater. **17**, 107 (2005).
[42] V. A. de la Peña O'Shea, P. R. de la Piscina, N. Homs, G. Aromí, and J. L. G. Fierro, Chem. Mater. **21**, 5637 (2009).
[43] L. Meziane, C. Salzemann, C. Aubert, H. Gérard, C. Petit, and M. Petit, Nanoscale **8**, 18640 (2016).
[44] G. Cheng, D. Romero, G. T. Fraser, and A. R. Hight Walker, Langmuir **21**, 12055 (2005).
[45] J. Zhao, M. Spasova, Z.-A. Li, and M. Zharnikov, Adv. Funct. Mater. **21**, 4724 (2011).
[46] Z. Zhang, X. Chen, X. Zhang, and C. Shi, Solid State Commun. **139**, 403 (2006).
[47] L. Liu, C. Qin, M. Yu, Q. Wang, J. Wang, B. Hou, L. Jia, and D. Li, ChemCatChem **12**, 2083 (2020).
[48] J. Thielsch, D. Suess, L. Schultz, and O. Gutfleisch, J. Appl. Phys. **114**, 223909 (2013).
[49] J. Mohapatra, M. Xing, J. Elkins, J. Beatty, and J. P. Liu, J. Phys. D: Appl. Phys. **53**, 504004 (2020).